Astrophysical Uncertainties in the Gravitational-Wave Background from Stellar-Mass Compact Binary Mergers

Leonard Lehoucq, Irina Dvorkin, Rahul Srinivasan, Clement Pellouin, Astrid Lamberts

Monthly Notices of the ROYAL ASTRONOMICAL SOCIETY

MNRAS **526,** 4378–4387 (2023) https://doi.org/10.1093/mnras/stad2917
Advance Access publication 2023 September 26

Astrophysical uncertainties in the gravitational-wave background from stellar-mass compact binary mergers

Léonard Lehoucq [1]★ Irina Dvorkin,[1]★ Rahul Srinivasan [2,3] Clément Pellouin[1] and Astrid Lamberts [2,3]

[1]*Institut d'Astrophysique de Paris, Sorbonne Université and CNRS, UMR 7095, 98 bis bd Arago, F-75014 Paris, France*
[2]*Observatoire de la Côte d'Azur, Université Côte d'Azur, CNRS, Lagrange, F-P789+P5 Nice France*
[3]*Observatoire de la Côte d'Azur, Université Côte d'Azur, CNRS, ARTEMIS, F-P789+P5 Nice France*

Accepted 2023 September 18. Received 2023 September 18; in original form 2023 June 19

ABSTRACT

We investigate the stochastic gravitational-wave background (SGWB) produced by merging binary black holes (BBHs) and binary neutron stars (BNSs) in the frequency ranges of Laser Interferometer Gravitational-Wave Observatory (LIGO)/Virgo/Kagra and *Laser Interferometer Space Antenna* (*LISA*). We develop three analytical models, which are calibrated to the measured local merger rates, and complement them with three population synthesis models based on the COSMIC code. We discuss the uncertainties, focusing on the impact of the BBH mass distribution, the effect of the metallicity of the progenitor stars, and the time delay distribution between star formation and compact binary merger. We also explore the effect of uncertainties in binary stellar evolution on the background. For BBHs, our analytical models predict $\Omega_{\rm GW}$ in the range [4×10^{-10} to 1×10^{-9}] (25 Hz) and [1×10^{-12} to 4×10^{-12}] (3 mHz), and between [2×10^{-10} to 2×10^{-9}] (25 Hz) and [7×10^{-13} to 7×10^{-12}] (3 mHz) for our population synthesis models. This background is unlikely to be detected during the LIGO/Virgo/Kagra O4 run, but could be detectable with *LISA*. We predict about 10 BBH and no BNS mergers that could be individually detectable by *LISA* for a period of observation of 4 yr. Our study provides new insights into the population of compact binaries and the main sources of uncertainty in the astrophysical SGWB.

Key words: gravitational waves – black hole mergers – neutron star mergers.

1 INTRODUCTION

Gravitational waves (GWs) have emerged as a promising tool for exploring our Universe (Abbott et al. 2016a). In recent years, ground-based detectors such as the Laser Interferometer Gravitational-Wave Observatory (LIGO) and Virgo have detected GWs from compact binary (CB) mergers. To date, a total number of 90 CB mergers with an inferred probability of astrophysical origin of $p_{\rm astro} > 0.5$ have been detected (Abbott et al. 2019a, 2021a, b, c, 2023). These observations have already provided valuable information about black hole (BH) and neutron star (NS) populations, in particular they have permitted to refine stellar population models that predict the formation and merger rates of CBs (e.g. Baibhav et al. 2019; Mapelli et al. 2019; Kimball et al. 2021; Zevin et al. 2021; Broekgaarden et al. 2022; van Son et al. 2022; Srinivasan et al. 2023).

In addition to these resolved signals from individual binary mergers, the incoherent superposition of unresolved sources creates an astrophysical stochastic GW background (SGWB). This signal, if detected, contains crucial information about high-redshift CB mergers. Moreover, other astrophysical and cosmological sources could contribute to the SGWB, including core-collapse supernovae, rotating NSs, primordial BHs, cosmological inflation, cosmic strings, and first-order phase transitions in the early Universe (see Regimbau 2011; Caprini & Figueroa 2018; Christensen 2019; Renzini et al. 2022, for extensive reviews).

The *Laser Interferometer Space Antenna* (*LISA*), a space-based interferometer to be launched in the next decade, aims to detect new classes of GW sources at mHz frequencies. One of the primary objectives of *LISA* is to detect a cosmological SGWB, which could, for example, be produced by phase transitions in the primordial Universe or by cosmic strings (Caprini & Figueroa 2018; Auclair et al. 2023). Most cosmological backgrounds are expected to be significantly lower in magnitude than the astrophysical one; however, some realistic cases rooted in particle physics, such as cosmic strings, predict signals that can be orders of magnitude larger (Auclair et al. 2020). None the less, investigating the properties of the astrophysical background is crucial in order to prepare the detection strategies of the cosmological signal (Chen, Huang & Huang 2019; Cusin et al. 2020; Zhao & Lu 2021; Liang et al. 2022).

The investigation of the SGWB is an active field of research, both theoretically and observationally. Data collected by the LIGO and Virgo observatories during the first three observational runs have been used to search for this background in the $\mathcal{O}(10)$–$\mathcal{O}(100)$ Hz range, but so far only upper limits have been inferred (Abbott et al. 2017, 2018a, b, 2019b, 2021d, e). The most stringent upper limit provided by the LIGO/Virgo collaboration in Abbott et al. (2021d) is $\Omega_{\rm GW} \leq 3.4 \times 10^{-9}$ at 25 Hz for a power-law background with a

★ E-mail: lehoucq@iap.fr (LL); dvorkin@iap.fr (ID)

spectral index of 2/3 (consistent with expectations for CB mergers). This limit is very likely to improve with the next observing runs of LVK and, in the more distant future, with 3G detectors (Einstein Telescope and Cosmic Explorer; Maggiore et al. 2020; Evans et al. 2021).

Models of SGWB from stellar-mass CBs have been studied in recent years with different methods, in particular using extrapolations of the local observed merger rate and BH mass distribution (e.g. Abbott et al. 2016b; Jenkins et al. 2018; Lewicki & Vaskonen 2021; Mukherjee & Silk 2021; Babak et al. 2023), analytical descriptions of BH formation and evolution via different channels, and including the effects of the metallicity of progenitor stars (e.g. Dvorkin et al. 2016; Nakazato, Niino & Sago 2016; Cusin et al. 2019; Mangiagli et al. 2019) as well as detailed population synthesis models (e.g. Périgois et al. 2021, 2022).

In this article, we explore the SGWB from binary BHs (BBHs) and binary NSs (BNSs), with a focus on the frequency ranges accessible to LIGO/Virgo and *LISA* and using both analytical and population synthesis models. We note that the recent work of Babak et al. (2023) has also addressed the SGWB from stellar-mass binaries in the *LISA* band. Our results, while using different astrophysical models, are in agreement with their conclusions, as we show below. Our goal here is to estimate the main sources of uncertainty stemming from astrophysical modelling and estimate the prospects of detection with LIGO/Virgo and *LISA*.

The structure of the article is as follows: Section 2 details all the ingredients we use to model the BBH and BNS populations, including mass, redshift, time delay, and metallicity distributions. Section 3 establishes our population synthesis models based on the COSMIC code (Breivik et al. 2020). Section 4 presents the calculation of the SGWB in the LIGO/Virgo and *LISA* frequency bands. Section 5 discusses the possibility for *LISA* to detect individually some of these sources. Finally, we discuss our results and their implications for future work in Section 6.

Throughout this article, we use the following cosmological parameters: $h_0 = H_0/H_{100} = 0.68$, where $H_{100} = 100\ \mathrm{km\,s^{-1}\,Mpc^{-1}}$, $\Omega_\Lambda = 0.69$, and $\Omega_\mathrm{m} = 0.31$ (Planck Collaboration VI 2020).

2 MODELLING THE BBH AND BNS POPULATIONS

This section describes all the components of our analytical modelling of the BBH and BNS populations. We leave the description of the population synthesis models to Section 3.

Each CB is represented by a set of six parameters: the masses M_1 and M_2 of the binary components (described in Section 2.1), the merger redshift of the CB (detailed in Section 2.2), its sky position represented by the right ascension α and the declination δ, and finally the orbital inclination angle θ. These three angles are drawn uniformly from the interval $[0, 2\pi]$ for α, and from $[-1, 1]$ for $\cos\delta$ and $\cos\theta$. We regroup as λ five parameters: $\lambda = \{M_1, M_2, \alpha, \delta, \theta\}$.

The spins χ_1 and χ_2 of the binary components are assumed to be zero as their effect is subdominant for the total energy in GWs emitted in the inspiralling phase (Zhou et al. 2023).

We assume that all CBs have circularized their orbits prior to entering the final phase of the inspiral. We note that while this assumption holds in the LIGO/Virgo band, this is not necessarily the case for *LISA*. Indeed, in some dynamical formation channels CBs enter the *LISA* band while still retaining some eccentricity (see, for example, Breivik et al. 2016).

2.1 Mass distributions

2.1.1 Black hole binaries

We introduce the following probability distributions to describe the masses of the binary components: $P(M_1)$ for the mass of the primary and $P(q)$ for the mass ratio $q = M_1/M_2$. In order to model these distributions, we use the LVK analysis of the third Gravitational-Wave Transient Catalog (GWTC-3; Abbott et al. 2023), based on the 69 confident BBH events that have a false alarm rate below $1\ \mathrm{yr}^{-1}$.

We have chosen to use mainly their POWERLAW + PEAK (PL + P) model, as it provides the highest Bayes factor among the models considered in the catalogue. We also discuss the impact of choosing other mass distributions, such as their POWERLAW (PL) and BROKEN POWERLAW (BPL) models. These models are described in the appendix of Abbott et al. (2023).

In the PL + P model (Talbot & Thrane 2018), the distribution of the primary mass M_1 has two components: a power law between m_min and m_max, and a Gaussian peak with mean μ_m and width σ_m. The parameter λ_peak determines the fraction of the BBH systems that are contained in the Gaussian peak. The full list of parameters and their best-fitting values are given in Abbott et al. (2023).

The $m_\mathrm{max} \sim 80\,\mathrm{M}_\odot$ cut-off is motivated by the pair-instability supernova (PISN) phenomenon. PISNe are thought to occur in very massive ($m_\mathrm{ZAMS} \gtrsim 130\ \mathrm{M}_\odot$) and low-metallicity ($Z \lesssim 0.1\ \mathrm{Z}_\odot$) stars (Fryer, Woosley & Heger 2001; Umeda & Nomoto 2002), in which electron–positron pair creation leads to a thermonuclear runaway that completely disrupts the star, leaving no remnant (Fryer et al. 2001; Woosley & Heger 2021). Previous calculations have suggested that this effect may create a mass gap in the BH mass distribution in the range of 50–130 $\mathrm{M}_\odot$ (Woosley & Heger 2021). The existence of this mass gap has been challenged by recent LIGO/Virgo observations that show BBH merging within the gap (Abbott et al. 2020a, d).

The Gaussian peak at $\mu_\mathrm{m} \sim 35\,\mathrm{M}_\odot$ could be explained by a similar phenomenon, but in less massive stars. In this case, the pair instability is not strong enough to completely disrupt the star, but can still lead to a transient regime where the star ejects matter to regain stability in a pulsating manner until its core eventually collapses (Fowler & Hoyle 1964; Umeda & Nomoto 2002). This pulsating PISN (PPISN) leaves a remnant BH, which is, however, less massive than it would have been in the absence of the pulsating mechanism.

Finally, the secondary mass M_2 is calculated from the mass ratio q, which has a probability density that is a power law with a smoothed cut at m_min (Abbott et al. 2023).

2.1.2 Neutron star binaries

The mass distribution of BNSs is obtained from Galactic observations and assumed to be valid at all redshifts. As per the study conducted by Farrow, Zhu & Thrane (2019), this distribution can be accurately represented by a Gaussian with a mean of 1.33 $\mathrm{M}_\odot$ and a standard deviation of 0.09 $\mathrm{M}_\odot$. We note that both NSs in the binary system are assumed to follow this mass distribution. The mass distribution of BNSs is not a critical parameter in this study as it is highly concentrated around a single value close to the Tolman–Oppenheimer–Volkoff limit, although this value is somewhat uncertain as it depends on the equation of state (Lattimer & Prakash 2016; Özel & Freire 2016; Abbott et al. 2018c).

It is important to note that the mass distribution of BNSs detected through GWs may differ from those observed in the Galaxy. This effect could indeed explain the observation of the BNS merger GW190425 (Abbott et al. 2020b; Romero-Shaw et al. 2020), whose

total mass is much larger than that of Galactic binaries. Additionally, the recent observation of GW190814 seems to have provided evidence for a BH–NS merger with a NS much heavier than typical Galactic NSs (Abbott et al. 2020c).

2.2 Redshift distributions

To compute the merger rate of CBs, we first use the star formation rate (SFR) ψ, as given in Vangioni et al. (2015) using a fit to observed data:

$$\psi(z) = \nu \frac{a\ \exp\left[b(z - z_{\rm m})\right]}{a - b + b\ \exp\left[a(z - z_{\rm m})\right]}\,, \tag{1}$$

with $\nu = 0.178\ {\rm M}_\odot\ {\rm Mpc}^{-3}\ {\rm yr}^{-1}$, $a = 2.37$, $b = 1.80$, and $z_{\rm m} = 2$.

We assume that the merger rate follows the SFR with some delay ($t_{\rm d}$), which represents the time between the formation of the stellar progenitors and the merger of the CBs. We also consider the metallicity Z, which plays a key role in the evolution of the binary and thus affects the merger rate, as detailed in Section 2.4. Thus, we can write the merger rate as

$$R_{\rm merg}(t) = \int_0^{Z_{\rm max}} \int_{t_{\rm d,min}}^{t_{\rm d,max}} \alpha(Z)\, \psi(t - t_{\rm d})\, P(t_{\rm d}|Z)\, P(Z|t - t_{\rm d})\, {\rm d}t_{\rm d}\, {\rm d}Z\,, \tag{2}$$

where α is the efficiency (in ${\rm M}_\odot^{-1}$) of forming CBs that merge within the age of the Universe. Although the general redshift dependence of this efficiency is not known, we can use the local merger rate of BBHs and BNSs measured by LIGO/Virgo (Abbott et al. 2023) to constrain its value, as described below in Section 2.5. Lastly, we take $Z_{\rm max} = Z_\odot = 0.014$, $t_{\rm d,max} = t_{\rm Hubble} = 13.8$ Gyr, and $t_{\rm d,min} = 10$ Myr.

Note that the time variable t in equation (2) is connected to the redshift z in equation (1) by

$$\frac{{\rm d}t}{{\rm d}z} = \frac{H_0^{-1}}{(1+z)\sqrt{\Omega_{\rm m}(1+z)^3 + \Omega_\Lambda}}\,. \tag{3}$$

In the following sections, we discuss each component of equation (2).

2.3 Time delay distributions

The time delay $t_{\rm d}$ between the formation of the stellar progenitors and the merger of the CBs can depend on their formation channel. It is usually assumed that the distribution of time delays is represented by a power-law probability function (e.g. Chruslinska et al. 2018, see the discussion in Section 2). In equation (2), we consider the possible dependence of $t_{\rm d}$ on the metallicity of the progenitor stars, which plays an important role in the formation of CB through its influence on the strength of the stellar winds. These processes are taken into account in population synthesis codes, which we discuss below.

In the following, we consider analytical models in which $t_{\rm d}$ does not depend on metallicity. Specifically, in the BASELINE model all time delays are taken to be zero, so that the CB merger rate follows the SFR, while in the BASELINE_DELAYS model the time delays are described by the probability distribution:

$$P(t_{\rm d}) \propto t_{\rm d}^{-1}\,. \tag{4}$$

This functional form closely follows the results of population synthesis codes, as seen in Fig. 1 below. This power law is restricted between 10 Myr and the Hubble time $t_{\rm Hubble}$.

Note that in both the BASELINE and the BASELINE_DELAYS model, the efficiency α in equation (2) is chosen to be constant.

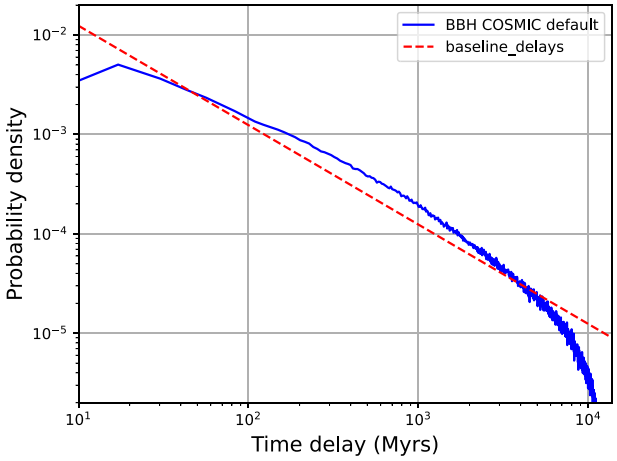

Figure 1. Time delay probability density integrated over all metallicities for our analytical BASELINE_DELAYS model and our COSMIC simulation with the default parameters. The power-law time delay model adopted in our analytical prescriptions provides a good description of the detailed COSMIC model.

2.4 Metallicity distributions

Metallicity affects the formation and evolution of BBHs in several ways. First, higher metallicity can result in more efficient stellar winds, which can decrease the final masses of the progenitor stars and affect the properties of the BBHs formed (Chruslinska, Nelemans & Belczynski 2019; Neijssel et al. 2019). Secondly, metallicity can impact the efficiency of mass transfer phases during binary star evolution (like the common envelope phase), which can result in less efficient mergers and a lower probability of forming BBHs (Neijssel et al. 2019). Finally, metallicity influences the properties of supernovae that produce BHs through fallback (Wong et al. 2014). In low-metallicity environments, the explosion mechanism is more likely to be asymmetric, leading to a larger fraction of BHs that receive a natal kick and thus breaking the binary. Additionally, the amount of mass ejected during a supernova is lower in low-metallicity environments, leading to the formation of more massive BHs (Belczynski et al. 2010; Spera, Mapelli & Bressan 2015).

Metallicity evolves with cosmic time as stars form and then enrich their surroundings with metals both during and at the end of their lifetimes. However, the metallicity distribution in the Universe is not homogeneous, with a large dispersion at any given redshift between various galaxies and even within individual galaxies. In our analytical models, at a given redshift we none the less use averaged quantities over the entire galactic population.

We take the metallicity evolution model from Belczynski et al. (2016):

$$\overline{Z}(z) = \frac{y(1-R)}{\rho_{\rm b}} \int_z^{z_{\rm max}} \frac{10^{0.5}\, \psi(z')}{H_0(1+z')\sqrt{\Omega_{\rm m}(1+z')^3 + \Omega_\Lambda}} {\rm d}z'\,, \tag{5}$$

where $R = 0.27$ is the return fraction (the mass fraction of each generation of stars that is ejected back into the interstellar medium), $y = 0.019$ is the net metal yield (the mass of new metals created and ejected into the interstellar medium by each generation of stars per unit mass locked in stars), and $\rho_{\rm b} = 2.77 \times 10^{11}\ \Omega_{\rm b} h_0\ {\rm M}_\odot\ {\rm Mpc}^{-3}$ is the baryon density, with $\Omega_{\rm b} = 0.045$.

We also include a dispersion in metallicity at any given redshift. Assuming for simplicity that this dispersion is lognormal (Santoliquido et al. 2021), we obtain the following probability distribution of

metallicity Z at redshift z:

$$P(Z|z) = \frac{1}{\sqrt{2\pi\sigma^2}} \exp\left(-\frac{(\log(Z/Z_\odot) - \log(\overline{Z}(z)/Z_\odot))^2}{2\sigma^2}\right), \tag{6}$$

with $\sigma = 0.2$. The probability $P(Z|t - t_d)$ that we use in equation (2) is then obtained using the redshift–time mapping of equation (3).

If we make the assumption that the probability $P(t_d|Z)$ in equation (2) does not depend on the metallicity, for example if it is a power law as considered in Section 2.3, then we can factorize the two integrals in the merger rate equation to obtain

$$R_{\rm merg}(t) = \int_{t_{\rm d,min}}^{t_{\rm d,max}} \psi(t - t_{\rm d})\, P(t_{\rm d})\, {\rm d}t_{\rm d} \;\times\; f_Z(t - t_{\rm d})\,, \tag{7}$$

with the merging fraction $f_Z(z(t))$:

$$f_Z(z(t)) = \int_0^{Z_{\rm max}} \alpha(Z)\, P(Z|z)\, {\rm d}Z\,. \tag{8}$$

We assume that no BHs could be formed by a progenitor star with a metallicity above 10 per cent of the solar one. This cut is inspired by population synthesis results (see e.g. Santoliquido et al. 2021; Srinivasan et al. 2023). As a result, under our assumptions, α is a step function centred on $Z_{\rm cut} = 0.1\ {\rm Z}_\odot$. Then $f_Z(z)$ is a step-like function with a cut-off around $z = 4.5$. The cut-off is sharpened with the decrease of σ in equation (6).

These metallicity effects are taken into account in our METALLICITY CUT model. Specifically, we use equation (7) to calculate the merger rate with the metallicity distribution given in equation (6) and the time delay distribution from equation (4). Note that for this model the time delay distribution is the same as for the BASELINE_DELAYS model, but the efficiency of forming CBs now depends on redshift.

2.5 Local rates and astrophysical uncertainty

In our analytical models, we do not know a priori the general redshift dependence of the efficiency α in equation (2). However, we can constrain its value by using the local merger rate obtained from the GWTC-3 catalogue by LIGO/Virgo (Abbott et al. 2023). That is, we take α constant in order that locally, the merger rate given in equation (2) matches the value measured by LIGO/Virgo.

For BBHs, we use the rate provided by the *PP* model in GWTC-3, which is $R_{\rm BBH}(z = 0.2) = 28.3^{+13.9}_{-9.1}\ {\rm yr}^{-1}\,{\rm Gpc}^{-3}$. This rate is given for $z = 0.2$ since it corresponds to the redshift where the uncertainty is minimal. For BNSs, we use the rate provided by the *PDB (pair)* model in GWTC-3, which is $R_{\rm BNS}(z = 0) = 44^{+96}_{-34}\ {\rm yr}^{-1}\,{\rm Gpc}^{-3}$. The uncertainties quoted for these values correspond to 90 per cent confidence intervals.

Note that, in our analytical models, we have assumed that the relevant quantities, such as the SFR, metallicity, time delay, mass, and redshift distribution, have already been averaged over the mass distribution of the host galaxies. This implies that the host galaxy dependence has been accounted for by taking an average over all possible hosts. This simplifies the analysis by eliminating the need to integrate the merger rate over the host galaxy mass distribution. However, we do not make this assumption for our BBH population synthesis model, as we detail in the next section.

3 POPULATION SYNTHESIS MODELS

We supplement the analytical models described above with a set of population synthesis models that rely on a more realistic description of stellar evolution. We follow the prescription of Srinivasan et al. (2023) to produce an astrophysical population of BBHs that merge by the present day. We account for the SFR through cosmic time as a function of progenitor environment properties (metallicity and galaxy mass) and the efficiency of BBH formation from binary stars. The former is adopted from the default SFR of Srinivasan et al. (2023) that models the mass–metallicity relation based on the metallicity calibration of Kobulnicky & Kewley (2004) and extrapolated to high redshift based on the fit provided by Ma et al. (2016). The latter is obtained using a rapid binary population synthesis code, COSMIC (v3.4.0; Breivik et al. 2020), which simulates the binary evolution of stars that ultimately form merging BBHs. These binary simulations are based on parametric models of single-star evolution and their binary interactions. We adopt the default binary evolution parameters shown in bold in table 1 of Srinivasan et al. (2023) to generate a population of merging BBHs, BBH COSMIC DEFAULT.

Uncertainties in modelling the SFR and binary evolution result in a large variance in the predicted merger rate. Therefore, we explore models with a pessimistic and optimistic merger rate in comparison to the BBH COSMIC DEFAULT, termed BBH COSMIC PESSIMISTIC and BBH COSMIC OPTIMISTIC, respectively. BBH COSMIC PESSIMISTIC differs from the default model in two aspects: a different critical mass ratio model of the onset of unstable mass transfer (qcflag = 4 as per COSMIC documentation[1] and a different common-envelope efficiency $\alpha = 0.1$). Likewise, BBH COSMIC OPTIMISTIC varies in the description of the common envelope phase (lambdaf = 0 and $\alpha = 0.2$ as per COSMIC documentation). The present-day merger rates of our PESSIMISTIC, DEFAULT, and OPTIMISTIC models are 15, 120, and 590 ${\rm Gpc}^{-3}\ {\rm yr}^{-1}$, respectively.

For the BNSs, we take the DEFAULT COSMIC parameters of Srinivasan et al. (2023). To compute the merger rate, we use equation (2) with SFR and metallicity distribution $P(Z|z)$ provided, respectively, in equations (1) and (6). We use 15 log-uniform metallicity bins between 4.4×10^{-4} and 2.8×10^{-1}. The mass efficiency $\alpha(Z)$ and the time delay distribution $P(t_d|Z)$ are calculated from our COSMIC results.

All of our models are summarized in Table 1. Analytical models (BASELINE, BASELINE_DELAYS, and METALLICITY CUT) are easy to calibrate and to use because of their small number of parameters. Each new analytical model adds a physical process (time delay, metallicity) that refines the model and makes it more realistic. None the less, these analytical models are not detailed enough and cannot capture some aspects of BBH and BNS formation. That is why we choose to compare them with more realistic models based on the population synthesis code COSMIC, as outlined above. This code describes better the physical processes at play during stellar

Table 1. Summary of our three analytical models and three population synthesis models. The PL + P BBH mass distribution is taken from Abbott et al. (2023). The ∅ symbol means that the model does not take into account the related parameter.

Model name	BBH mass dist.	Time delay dist.	Metallicity
BASELINE	PL + P	∅	∅
BASELINE_DELAYS	PL + P	Power law, equation (4)	∅
METALLICITY CUT	PL + P	Power law, equation (4)	Equations (7) and (8)
COSMIC	Three models: DEFAULT, PESSIMISTIC, and OPTIMISTIC. They have different sets of parameters (described in Section 3) that change the stellar evolution.		

[1] https://cosmic-popsynth.github.io/

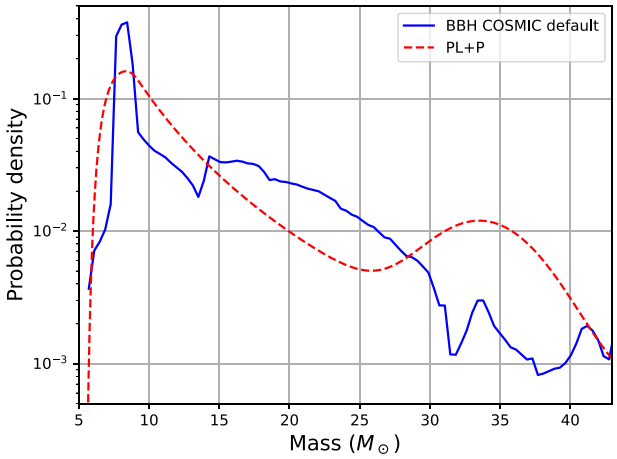

Figure 2. The distribution of the primary mass M_1 for the PL + P model from the GWTC-3 catalogue and our COSMIC simulations with default parameters. The peak at around $M_1 \sim 10\ \mathrm{M}_\odot$ as well as the power-law-like behaviour are similar in both models. Note, however, the differences at high masses, at $M_1 \gtrsim 30\ \mathrm{M}_\odot$.

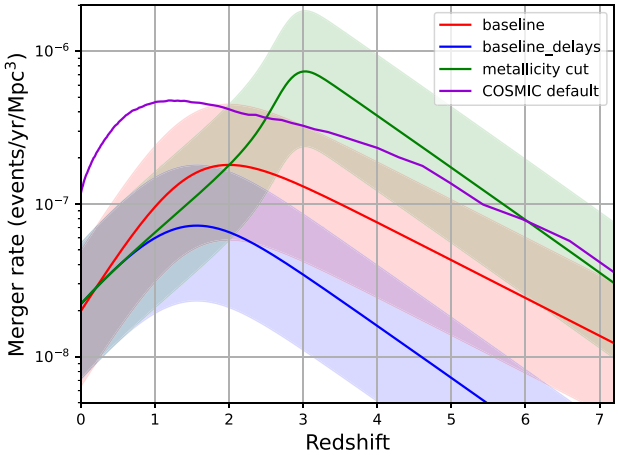

Figure 3. The merger rate of BBHs calculated with our main models. The uncertainties in this figure come from the 90 per cent confidence interval on the merger rate at $z = 0.2$ from the GWTC-3 catalogue. We assume the uncertainty to be the same at every redshift.

evolution, taking into account several physical effects (common envelope phase, kick velocity, etc.; see Breivik et al. 2020) and it is in this sense more realistic. On the other hand, population synthesis codes have numerous parameters that are difficult to constrain (see Mandel & Broekgaarden 2022, for a recent review). Looking at observables produced by a set of COSMIC parameters (for example, BBH merger rate and stochastic backgrounds) and comparing them to observations could help us to calibrate COSMIC parameters. In practice, there are currently not enough observational constraints to overcome the degeneracies between various COSMIC parameters. In this work, we are not attempting to calibrate COSMIC parameters, rather we use specific sets of parameters that represent well the range of variability of COSMIC.

In Fig. 2, we show the BBH primary mass distribution of the PL + P model and the one resulting from our default COSMIC model. The COSMIC distribution has a more pronounced peak at low masses around 8 $\mathrm{M}_\odot$ and presents an overdensity centred around 22 $\mathrm{M}_\odot$ but does not have any peak around 34 $\mathrm{M}_\odot$ contrary to the PL + P model.

Fig. 1 compares the time delay probability density integrated over all metallicities in our analytical BASELINE_DELAYS model and our default COSMIC model. The distribution from COSMIC is very close to a power law but with a turn over at very short time delays.

We compare the merger rate of BBHs in our models in Fig. 3. As expected, since there is no time delay between formation and merger, the shape of the BASELINE merger rate is close to the SFR (see equation 1) and peaks at around $R_{\mathrm{merg}}(z = 2) \sim 1.5 \times 10^7$ events $\mathrm{yr}^{-1}\ \mathrm{Mpc}^{-3}$.

We also observe that for $z > 0.2$ the BASELINE_DELAYS merger rate is always below the BASELINE model. The reason is that the inclusion of time delays shifts the entire BASELINE merger rate curve to lower redshifts. Then this shifted curve needs to be renormalized to be in accordance with the local LIGO/Virgo observations at $z = 0.2$, as described in Section 2.5. This procedure then results in a merger rate that is below the BASELINE model at all redshifts above $z = 0.2$.

The merger rate in the METALLICITY CUT model is slightly lower than the BASELINE one at small redshifts ($z < 2$), but significantly higher at larger redshifts ($z > 2$). This is due to the fact that the effect of metallicity is to reduce the fraction of massive stars that can collapse into BHs. At lower redshifts, stars tend to have higher metallicity, resulting in fewer stars collapsing into BHs. Conversely, at higher redshifts, stars tend to have lower metallicity, leading to a larger fraction of stars collapsing into BHs. The asymmetry of this trend around the BASELINE model results predominantly from the renormalization of the merger rate at low redshifts ($z = 0.2$).

Finally, the merger rate from the COSMIC DEFAULT model is significantly higher than our other models and peaks at lower redshift around $z = 1$. This model predicts a merger rate at $z = 0.2$, which is outside the 90 per cent confidence interval computed in the GWTC-3 catalogue (Abbott et al. 2023). This implies that the default set of parameters from Srinivasan et al. (2023) does not describe the observed merger rate of BBHs. Note that this difference in merger rate can be also due to our model for star formation and metallicity evolution.

In this study, we choose to explore the range of uncertainties due to COSMIC parameters rather than trying to find the best parameter set. For this reason, we include also two other sets (PESSIMISTIC and OPTIMISTIC in Table 1) from the same study that represent well the range of variability of COSMIC models. The former set has a merger rate at $z = 0.2$ that is in accordance with GWTC-3, while the latter provides an upper bound on the merger rate that COSMIC can predict.

4 CALCULATION OF THE SGWB FROM BBH AND BNS

The total dimensionless energy density of GWs Ω_{GW}, per logarithmic unit of frequency and in unit of the critical density of the Universe ρ_{c}, is expressed as

$$\Omega_{\mathrm{GW}} = \frac{1}{\rho_{\mathrm{c}}} \frac{\mathrm{d}\rho_{\mathrm{GW}}}{\mathrm{d}\ln f}\,, \tag{9}$$

with $\mathrm{d}\rho_{\mathrm{GW}}$ the energy density of the GWs in the frequency interval $[f, f + \mathrm{d}f]$.

We can write the background from BBH or BNS mergers as

$$\Omega_{\mathrm{GW}}(f) = \frac{f}{\rho_{\mathrm{c}} c^2 H_0} \int_0^{z_{\mathrm{max}}} \int_\lambda \frac{R_{\mathrm{merg}}(z, \lambda)\, \frac{\mathrm{d}E_{\mathrm{GW}}(f_{\mathrm{s}})}{\mathrm{d}f_{\mathrm{s}}}\, P(\lambda)}{(1+z)\sqrt{\Omega_{\mathrm{M}}(1+z)^3 + \Omega_\Lambda}}\, \mathrm{d}\lambda\, \mathrm{d}z\,, \tag{10}$$

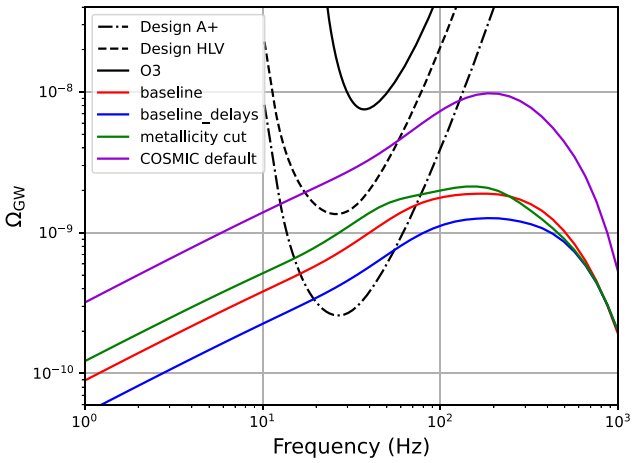

Figure 4. In coloured lines, the SGWB from BBHs calculated with our main models (see Table 1); in black lines, the LIGO/Virgo SGWB sensibility. There is a factor of 3 variability in the background predicted by our analytical models. The prediction obtained using COSMIC DEFAULT significantly exceeds the analytical models, mainly due to its higher merger rate (see Fig. 3).

with f the observed frequency, $f_s = f\,(1+z)$ the frequency emitted at the source, $R_{\rm merg}$ the CB merger rate, $\mathrm{d}E_{\rm GW}(f_s)/\mathrm{d}f_s$ the energy spectrum emitted by each CB, and $P(\lambda)$ the probability distribution of the parameters of the CB, summarized as λ.

We used the phenomenological expression given in Périgois et al. (2021) for the energy spectrum emitted by each CB. The coefficients of this expression are obtained by matching post-Newtonian and numerical relativity waveforms (see Appendix A and Ajith et al. 2011).

4.1 LIGO/Virgo and *LISA* sensitivity to an SGWB

We use the LIGO/Virgo sensitivity curves to an SGWB given by the LIGO/Virgo/Kagra collaboration (Abbott et al. 2023). For *LISA*, we use an analytical approximation for the sensitivity curve for a point-like source given in Robson, Cornish & Liu (2019) to calculate the power-law integrated sensitivity to an SGWB.

We define the latter to be the limit at which the signal-to-noise ratio (SNR) for detecting a signal is equal to 5, assuming an observation time of $T_{\rm obs} = 4$ yr. A reasonable frequency range to calculate the sensitivity of *LISA* is between 10^{-1} and 10^{2} mHz. To compute the power-law integrated sensitivity curve, we use the method proposed by Thrane & Romano (2013).

5 STELLAR-MASS CB MERGERS DETECTABLE BY *LISA*

Even though the mergers of stellar-mass BHs do not emit their maximum intensity in the *LISA* band, it could be possible to detect these systems individually with *LISA*. In fact, *LISA* is not well suited to detect stellar-mass BBH and BNS because its sensibility is in the mHz regime. None the less, by accumulating the signal over multiple periods, the SNR can be increased and pass beyond the detection threshold. We estimate the expected number of individual detections $N_{\rm LISA}$ with *LISA* for a mission duration of $T_{\rm obs} = 4$ yr using the method described in Gerosa et al. (2019):

$$N_{\rm LISA} = \int_z \int_\lambda P(\lambda)\, R_{\rm merg}(z)\, \frac{\mathrm{d}V_c}{\mathrm{d}z}\, \frac{1}{1+z}\, \Delta(\lambda, z)\, \mathrm{d}z\, \mathrm{d}\lambda\,. \tag{11}$$

The quantity $\Delta(\lambda, z)$ provides an estimate of the time window in which a merging CB is visible by *LISA* with SNR above a threshold value $\mathrm{SNR}_{\rm thr}$. We chose $\mathrm{SNR}_{\rm thr} = 8$ since the source parameters were shown to be well constrained in this case (Buscicchio et al. 2021), although we note that lower values can be considered for sources observable with ground-based detectors (Wong et al. 2018).

We need to remove these sources from the background, since they are individually detected. Removing these sources will lower the background, thus some new sources could become individually detectable since the background contributes to the overall noise budget. As a result, Δ in equation (11) is likely to increase with the decrease of the background. Therefore, we need to recompute $N_{\rm LISA}$ and eventually repeat this process until we reach convergence. In practice, this iterative process is not necessary, indeed in our case $N_{\rm LISA}$ is of the order of magnitude of 10 for the BBHs and 0 for the BNSs (see the results in Section 6 below). Thus, detectable stellar-mass sources have a negligible contribution to the SGWB for *LISA*.

6 RESULTS

In this section, we present and analyse the results of the various models for the SGWB from BBH and BNS sources, in both the *LISA* and LIGO/Virgo frequency ranges. The main results are summarized in Fig. 4 and Table 2, which provides the SGWB values at 3 mHz and 25 Hz, which are the reference frequencies, respectively, for *LISA* and LIGO/Virgo. All of our models are consistent with the upper limit from LVC O3 observations, but only the COSMIC model predicts an SGWB strong enough to be confidently detected with design LIGO/Virgo sensitivity.

Compared to the BASELINE model, the BASELINE_DELAYS takes into account the time delay of the CB mergers, leading to a decrease in the SGWB by a factor of 1.7 across all frequencies. Indeed, as we showed

Table 2. Values of the SGWB in Fig. 4 and the number of the individually detected BBH mergers with *LISA* with an SNR of at least 8 for a 4 yr observation run. $N_{\rm LISA} \sim 10$ for all of our analytical models. The error bars on the background from analytical models come from the 90 per cent confidence interval on the merger rate at $z = 0.2$ (GWTC-3 catalogue), on which these models are calibrated. Error bars cannot be provided for population synthesis-based models, but in Fig. 5 and in the text we discuss their range of uncertainty.

Models	BASELINE	BASELINE_DELAYS	Z CUT	COSMIC
(25 Hz) $\Omega_{\rm GW} \times 10^{10}$	$6.83^{+3.35}_{-2.20}$	$3.99^{+1.96}_{-1.28}$	$9.42^{+4.63}_{-3.03}$	24.11
(3 mHz) $\Omega_{\rm GW} \times 10^{12}$	$1.89^{+0.93}_{-0.61}$	$1.10^{+0.54}_{-0.35}$	$2.61^{+1.28}_{-0.84}$	6.75
$N_{\rm LISA}$	6^{+3}_{-2}	7^{+3}_{-2}	7^{+3}_{-2}	19

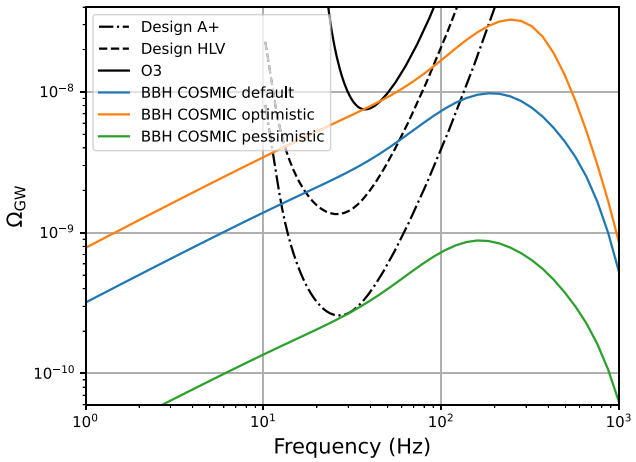

Figure 5. The SGWB from BBHs, based on the results of our COSMIC simulations discussed in Section 3. There is a variation of one order of magnitude between our models. The COSMIC OPTIMISTIC model seems to be already excluded by observation, since no background has been detected during O3.

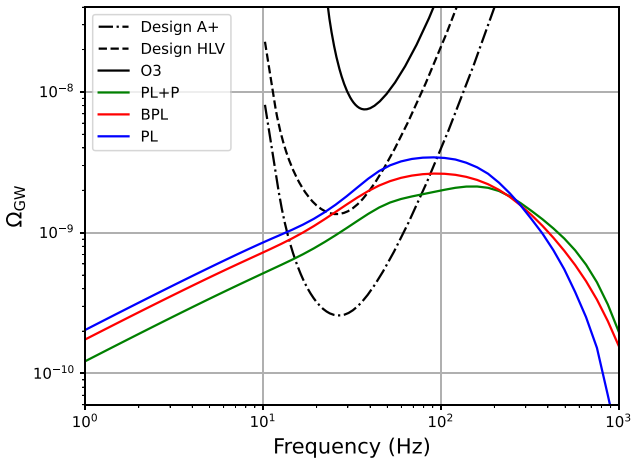

Figure 6. The SGWB for BBH mass distribution models described in Abbott et al. (2023) and the METALLICITY CUT model. Varying the mass distribution results in a factor of 2 difference of the SGWB.

in Section 3, the BASELINE_DELAYS merger rate is lower compared to the BASELINE at all redshifts, resulting in a lower background since the other parameters in equation (10) remain unchanged for both of these models.

The METALLICITY CUT model includes the effect of metallicity, resulting in an amplitude increase by a factor of 1.4 and a shift of the peak towards lower frequencies. These effects can be explained by the combination of two effects. First, as shown in Section 3, the METALLICITY CUT merger rate is higher than the BASELINE one for most of the redshift range, thus the corresponding background is higher. Secondly, as can be seen in Fig. 3, the merger rate for the METALLICITY CUT model peaks close to $z = 3$. As a result, the GW frequencies of the background for this model are more redshifted.

Note that a second bump is observed in the METALLICITY CUT merger rate around 50 Hz. As we show below, this feature is due to the peak in the PL + P mass distribution.

The SGWB obtained for the COSMIC model is higher than that for the other models, and so upcoming observations in run O4 are expected to have sufficient sensitivity to either detect or place strong constraints on this model. It is important to mention that the peak around 200 Hz in the COSMIC model appears to be more prominent than in other cases. This is due to the mass distribution produced by the COSMIC simulation, which peaks at lower masses than the distribution presented in GWTC-3 (Abbott et al. 2023), as shown in Fig. 1.

Fig. 5 compares the results of the three different COSMIC runs described in Section 3. We choose these runs because they illustrate well the range of uncertainty of binary population synthesis models. It can be seen that changing the stellar evolution parameters of the COSMIC code leads to a variation of one order of magnitude in the resulting background, from the O3 limits to the design sensitivity. Therefore, the range predicted by the COSMIC models studied in this paper will be probed in the near future. In fact, the OPTIMISTIC model appears to be already excluded by observations, as no background has been detected during O3. Thus, this also excludes the merger rate predicted by this model. The upcoming O4 run is expected to constrain even more these parameters.

In Fig. 6, we set the model to be METALLICITY CUT, and we examine the impact of the mass distribution model on the background. The

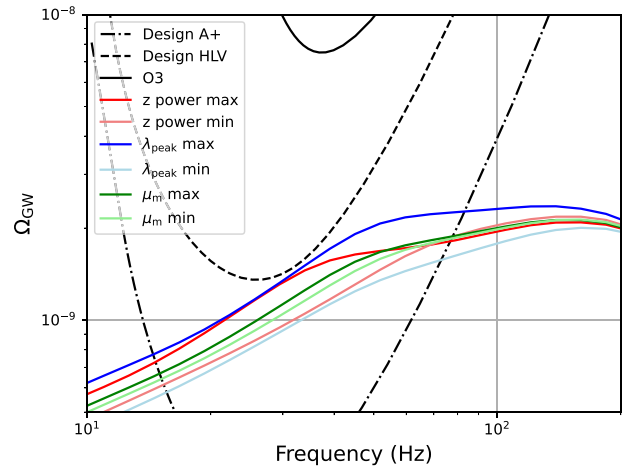

Figure 7. The variation of the SGWB from BBHs due to uncertainties on the PL + P mass distribution. Each coloured curve represents the predicted background by our METALLICITY CUT model with each time a different value for one parameter of the PL + P distribution. The uncertainty on the amplitude of the Gaussian peak of the PL + P model results in the most significant variation on the background.

PL + P distribution results in a broad peak with two distinguishable bumps around 50 and 200 Hz, which are a result of the two peaks in this mass distribution (around 5 and 35 $M_\odot$). On the other hand, the PL model gives only one peak around 100 Hz and a bit higher background overall. The BPL model is intermediate between the two, with a lower background but a wider peak. Upcoming O4 observations have the potential to constrain the parameters of the mass distribution models and thus the resulting background.

Fixing the mass model to be PL + P, we now study the impact of the main parameters of this mass distribution on the resulting background. To this end, we vary the amplitude (λ_{peak}) and the position (μ_m) of the Gaussian peak in the mass distribution. These values are set to their maximum and minimum of the 90 per cent credibility interval, and the resulting backgrounds are compared in Fig. 7.

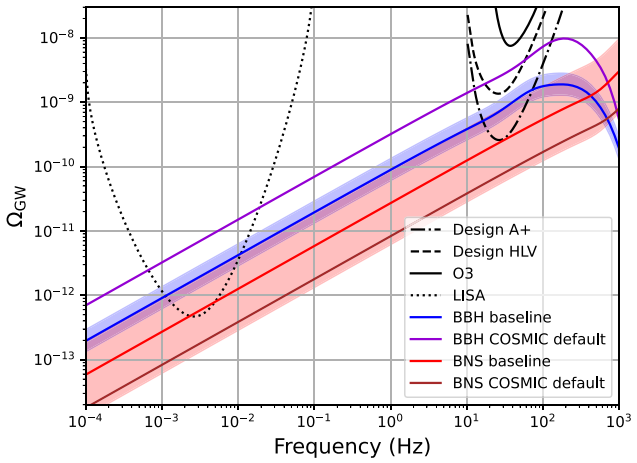

Figure 8. The SGWB from both BBHs and BNSs in the frequency range of *LISA* and LIGO/Virgo. The analytical and population synthesis models for the BNS background are compatible, within the error bars of the former, contrary to their predictions for the BBH.

Table 3. Our predictions for the SGWB in LIGO/Virgo and *LISA* frequency bands, comparing the BASELINE and default COSMIC models.

	BBH		BNS	
Models	BASELINE	COSMIC	BASELINE	COSMIC
(25 Hz) $\Omega_{GW} \times 10^{10}$	6.83	24.11	2.07	1.60
(3 mHz) $\Omega_{GW} \times 10^{12}$	1.89	6.75	0.52	0.40

We also investigate the impact of varying μ_m with redshift by taking $\mu_m \propto (1+z)^{0.5}$ ('z power max' in Fig. 7) or $\mu_m \propto (1+z)^{-0.5}$ ('z power min'). Indeed, μ_m may vary with the redshift since, as we discuss in Section 2.1, the Gaussian peak in the mass distribution could be the result of PPISNe and the efficiency of this phenomenon depends on the metallicity (and so on the redshift).

The uncertainty in the amplitude of the peak results in the most significant variations of the SGWB. When set to its minimum, the bump around 50 Hz is almost imperceptible. The uncertainty in the absolute position of μ_m results in only minor variations in the background. However, assuming a strong redshift dependence moves the bump from 35 ('z power max') to 75 Hz ('z power min').

Note that the bump in the background around 200 Hz does not change. This confirms that the secondary bump around 50 Hz is indeed due to the peak around 35 $M_\odot$ in the PL + P mass distribution. Furthermore, this secondary bump is the closest part of the SGWB to the minimum sensitivity of LIGO/Virgo and thus could be one of the first features of the SGWB to be detected.

In Fig. 8 and Table 3, we compare the backgrounds due to BBH and BNS mergers for the BASELINE and the DEFAULT COSMIC models. The uncertainty bands for the BASELINE model are based on the 90 per cent credibility interval of the local merger rate measurement by LIGO/Virgo, as reported in Abbott et al. (2023), and are consistent with the recent results reported in Babak et al. (2023). Our results show that the default parameters of COSMIC are not in agreement with the simple analytical model for the BBH background (this is not so surprising since the merger rates predicted by these models are perceptibly different, see Fig. 3). However, this is not the case for the BNS background. It is important to note that the uncertainty for the BNS case is very high given that LIGO/Virgo have only detected two BNS mergers to date. The fourth run of LIGO/Virgo is expected to detect a few additional BNS mergers (Colombo et al. 2022), which will result in a more constrained local merger rate. Finally, our results suggest that the BNS background is likely subdominant to the BBH contribution, consistent with previous studies.

7 CONCLUSION

We investigated the SGWB produced by several population models of BBHs and BNSs in the frequency ranges of LIGO/Virgo and *LISA*. We developed three analytical models, namely BASELINE, BASELINE_DELAYS, and METALLICITY CUT, and complemented them with a set of population synthesis models based on the COSMIC code. Our BASELINE model assumes a merger rate that follows the SFR with zero delay times, while the BASELINE_DELAYS model takes into account the time delay between the formation of the stellar progenitors and the merger of the CBs. The METALLICITY CUT model includes also the effect of metallicity on the efficiency of producing CBs.

We specifically focused on the mass distribution of CBs in our models. For BBHs, we used mainly the PL + P mass distribution from GWTC-3 and investigated some other distributions from the same catalogue. For BNSs, we used the mass distribution obtained from Galactic observations, assumed to be valid at all redshifts.

To complement our analytical models, we investigated three models for the BBH population based on the population synthesis code COSMIC, which differ by the set of parameters used to describe the stellar physics, namely OPTIMISTIC, PESSIMISTIC, and DEFAULT. The mass distribution predicted by the COSMIC models differs from the PL + P model, but the time delay distribution was consistent with a simple power law as used in our analytical description. For BNSs, we used only one COSMIC simulation with the DEFAULT set of parameters.

For BBHs, our analytical models predict Ω_{GW} in the range [4 $\times$ 10^{-10} to 1 $\times$ 10^{-9}] at 25 Hz and [1 $\times$ 10^{-12} to 4 $\times$ 10^{-12}] at 3 mHz, where the range of our predicted values corresponds to the uncertainty in the physical assumptions of our models. These backgrounds could be detectable by *LISA* with a period of observation of 4 yr, but they are unlikely to be detected during the upcoming LIGO/Virgo/Kagra O4 run. However, the O4 run can help to constrain the parameters of our models.

Our analytical models are calibrated to the observed merger rate at $z = 0.2$. Thus, the uncertainty in this measurement can lead to a possible variation of about a factor of 1.5 for BBHs and 2 for BNSs in the predicted background.

We also investigated the impact of the mass distribution of BBHs on the background, which could vary by a factor of 2 by varying the mass distribution model within the confidence limits of the GWTC-3 population analysis. Additionally, we found that the uncertainties of the Gaussian peak of the PL + P mass distribution are dominated by the uncertainty in the amplitude of this peak and could lead to a factor of 1.5 variation in the SGWB. We also discussed the possibility that the position of this peak depends on redshift, but more constraints on the amplitude are needed in order to explore this potential effect. Indeed, our results suggest that the main source of uncertainty is the amplitude of the peak, while its redshift dependence has a negligible impact on the amplitude of the SGWB.

The SGWB predicted by our three COSMIC models varies between [2 $\times$ 10^{-10} to 2 $\times$ 10^{-9}] (25 Hz) and [7 $\times$ 10^{-13} to 7 $\times$ 10^{-12}] (3 mHz). This range, which is larger than the uncertainty due to the measurement error of the local merger rate, corresponds to the uncertainties in the physics of massive stellar binaries (Srinivasan

et al. 2023). The OPTIMISTIC COSMIC model appears to be excluded by observations, as no background has been detected during O3. However, the upcoming O4 run will likely help us constrain the parameters of the stellar model.

Finally, all of our models predict an O(10) number of BBHs and no BNSs that could be individually detectable by *LISA* for a period of observation of 4 yr.

While we have explored some uncertainties in the SGWB from CBs, several important effects were not included and could lead to further variations in the predicted SGWB. First, we assumed that all binaries are circularized; however, including eccentricity and precession in the waveforms might have an important effect on the SGWB amplitude (Zhao & Lu 2021).

More importantly, in this study we considered only the isolated binary formation scenario for BBHs, while the properties of the observed BBH population suggest that some sources could be formed through the dynamical channel, in particular hierarchical mergers in dense stellar environments. The mass and redshift distributions of this population are expected to be quite different and lead to a different component of the SGWB (Périgois et al. 2022). The remnants of Pop III stars, which could have higher merger rates at higher redshifts, could also have an important contribution to the SGWB (Dvorkin et al. 2016; Hartwig et al. 2016; Martinovic et al. 2022). These contributions and their associated uncertainties will be studied in future work.

ACKNOWLEDGEMENTS

This work was supported by the Programme National des Hautes Energies of CNRS/INSU with INP and IN2P3, co-funded by CEA and CNES. We thank Cyril Pitrou and Jean-Philippe Uzan for their very useful comments and all the interesting discussions we had together. CP acknowledges funding support from the Initiative Physique des Infinis (IPI), a research training programme of the Idex SUPER at Sorbonne Université. RS and AL acknowledge support from the graduate and research school EUR SPECTRUM. This work made use of the Infinity computing cluster at IAP.

DATA AVAILABILITY

The data underlying this article will be shared on reasonable request to the corresponding author.

REFERENCES

Abbott B. P. et al., 2016a, Phys. Rev. Lett., 116, 061102
Abbott B. P. et al., 2016b, Phys. Rev. Lett., 116, 131102
Abbott B. P. et al., 2017, Phys. Rev. Lett., 118, 121101
Abbott B. P. et al., 2018a, Phys. Rev. Lett., 120, 091101
Abbott B. P. et al., 2018b, Phys. Rev. Lett., 120, 201102
Abbott B. P. et al., 2018c, Phys. Rev. Lett., 121, 161101
Abbott B. P. et al., 2019a, Phys. Rev. X, 9, 031040
Abbott B. P. et al., 2019b, Phys. Rev. D, 100, 061101
Abbott R. et al., 2020a, Phys. Rev. Lett., 125, 101102
Abbott R. et al., 2020b, ApJ, 892, L3
Abbott R. et al., 2020c, ApJ, 896, L44
Abbott R. et al., 2020d, ApJ, 900, L13
Abbott R. et al., 2021a, preprint (arXiv:2108.01045)
Abbott R. et al., 2021b, preprint (arXiv:2111.03606)
Abbott R. et al., 2021c, Phys. Rev. X, 11, 021053
Abbott R. et al., 2021d, Phys. Rev. D, 104, 022004
Abbott R. et al., 2021e, Phys. Rev. D, 104, 022005
Abbott R. et al., 2023, Phys. Rev. X, 13, 011048
Ajith P. et al., 2008, Phys. Rev. D, 77, 104017
Ajith P. et al., 2011, Phys. Rev. Lett., 106, 241101
Auclair P. et al., 2020, J. Cosmol. Astropart. Phys., 2020, 034
Auclair P. et al., 2023, Living Rev. Relativ., 26, 5
Babak S. et al., 2023, J. Cosmol. Astropart. Phys., 2023, 034
Baibhav V., Berti E., Gerosa D., Mapelli M., Giacobbo N., Bouffanais Y., Di Carlo U. N., 2019, Phys. Rev. D, 100, 064060
Belczynski K., Dominik M., Bulik T., O'Shaughnessy R., Fryer C., Holz D. E., 2010, ApJ, 715, L138
Belczynski K., Holz D. E., Bulik T., O'Shaughnessy R., 2016, Nature, 534, 512
Breivik K., Rodriguez C. L., Larson S. L., Kalogera V., Rasio F. A., 2016, ApJ, 830, L18
Breivik K. et al., 2020, ApJ, 898, 71
Broekgaarden F. S. et al., 2022, MNRAS, 516, 5737
Buscicchio R., Klein A., Roebber E., Moore C. J., Gerosa D., Finch E., Vecchio A., 2021, Phys. Rev. D, 104, 044065
Caprini C., Figueroa D. G., 2018, Class. Quantum Gravity, 35, 163001
Chen Z.-C., Huang F., Huang Q.-G., 2019, ApJ, 871, 97
Christensen N., 2019, Rep. Prog. Phys., 82, 016903
Chruslinska M., Belczynski K., Klencki J., Benacquista M., 2018, MNRAS, 474, 2937
Chruslinska M., Nelemans G., Belczynski K., 2019, MNRAS, 482, 5012
Colombo A., Salafia O. S., Gabrielli F., Ghirlanda G., Giacomazzo B., Perego A., Colpi M., 2022, ApJ, 937, 79
Cusin G., Dvorkin I., Pitrou C., Uzan J.-P., 2019, Phys. Rev. D, 100, 063004
Cusin G., Dvorkin I., Pitrou C., Uzan J.-P., 2020, MNRAS, 493, L1
Dvorkin I., Vangioni E., Silk J., Uzan J.-P., Olive K. A., 2016, MNRAS, 461, 3877
Evans M. et al., 2021, preprint (arXiv:2109.09882)
Farrow N., Zhu X.-J., Thrane E., 2019, ApJ, 876, 18
Fowler W. A., Hoyle F., 1964, ApJS, 9, 201
Fryer C. L., Woosley S. E., Heger A., 2001, ApJ, 550, 372
Gerosa D., Ma S., Wong K. W. K., Berti E., O'Shaughnessy R., Chen Y., Belczynski K., 2019, Phys. Rev. D, 99, 103004
Hartwig T., Volonteri M., Bromm V., Klessen R. S., Barausse E., Magg M., Stacy A., 2016, MNRAS, 460, L74
Jenkins A. C., Sakellariadou M., Regimbau T., Slezak E., 2018, Phys. Rev. D, 98, 063501
Kimball C. et al., 2021, ApJ, 915, L35
Kobulnicky H. A., Kewley L. J., 2004, ApJ, 617, 240
Lattimer J. M., Prakash M., 2016, Phys. Rep., 621, 127
Lewicki M., Vaskonen V., 2021, preprint (arXiv:2111.05847)
Liang Z.-C., Hu Y.-M., Jiang Y., Cheng J., Zhang J.-d., Mei J., 2022, Phys. Rev. D, 105, 022001
Ma X., Hopkins P. F., Faucher-Giguère C.-A., Zolman N., Muratov A. L., Kereš D., Quataert E., 2016, MNRAS, 456, 2140
Maggiore M. et al., 2020, J. Cosmol. Astropart. Phys., 2020, 050
Mandel I., Broekgaarden F. S., 2022, Living Rev. Relativ., 25, 1
Mangiagli A., Bonetti M., Sesana A., Colpi M., 2019, ApJ, 883, L27
Mapelli M., Giacobbo N., Santoliquido F., Artale M. C., 2019, MNRAS, 487, 2
Martinovic K., Périgois C., Regimbau T., Sakellariadou M., 2022, ApJ, 940, 29
Mukherjee S., Silk J., 2021, MNRAS, 506, 3977
Nakazato K., Niino Y., Sago N., 2016, ApJ, 832, 146
Neijssel C. J. et al., 2019, MNRAS, 490, 3740
Özel F., Freire P., 2016, ARA&A, 54, 401
Périgois C., Belczynski C., Bulik T., Regimbau T., 2021, Phys. Rev. D, 103, 043002
Périgois C., Santoliquido F., Bouffanais Y., Di Carlo U. N., Giacobbo N., Rastello S., Mapelli M., Regimbau T., 2022, Phys. Rev. D, 105, 103032
Planck Collaboration VI, 2020, A&A, 641, A6
Regimbau T., 2011, Res. Astron. Astrophys., 11, 369
Renzini A. I., Goncharov B., Jenkins A. C., Meyers P. M., 2022, Galaxies, 10, 34
Robson T., Cornish N. J., Liu C., 2019, Class. Quantum Gravity, 36, 105011

Romero-Shaw I. M., Farrow N., Stevenson S., Thrane E., Zhu X.-J., 2020, MNRAS, 496, L64
Santoliquido F., Mapelli M., Giacobbo N., Bouffanais Y., Artale M. C., 2021, MNRAS, 502, 4877
Spera M., Mapelli M., Bressan A., 2015, MNRAS, 451, 4086
Srinivasan R., Lamberts A., Bizouard M. A., Bruel T., Mastrogiovanni S., 2023, MNRAS, 524, 60
Talbot C., Thrane E., 2018, ApJ, 856, 173
Thrane E., Romano J. D., 2013, Phys. Rev. D, 88, 124032
Umeda H., Nomoto K., 2002, ApJ, 565, 385
van Son L. A. C. et al., 2022, ApJ, 931, 17
Vangioni E., Olive K. A., Prestegard T., Silk J., Petitjean P., Mandic V., 2015, MNRAS, 447, 2575
Wong T.-W., Fryer C. L., Ellinger C. I., Rockefeller G., Kalogera V., 2014, preprint (arXiv:1401.3032)
Wong K. W. K., Kovetz E. D., Cutler C., Berti E., 2018, Phys. Rev. Lett., 121, 251102
Woosley S. E., Heger A., 2021, ApJ, 912, L31
Zevin M. et al., 2021, ApJ, 910, 152
Zhao Y., Lu Y., 2021, MNRAS, 500, 1421
Zhou B., Reali L., Berti E., Çalışkan M., Creque-Sarbinowski C., Kamionkowski M., Sathyaprakash B. S., 2023, Phys. Rev. D, 108, 064040

APPENDIX

The energy loss of a binary system by gravitational radiation is expressed according to the three phases of the coalescence, the inspiralling phase (for $f_s < f_{merg}$), the coalescence phase (for $f_{merg} \leq f_s < f_{ring}$), and finally the ringdown phase, i.e. the relaxation phase (for $f_{ring} \leq f_s < f_{cut}$). It is therefore expressed as (Ajith et al. 2008)

$$\frac{dE_{GW}(f_s)}{df_s} = \frac{dE_{GW}^{Newton}(f_s)}{df_s} \times \begin{cases} (1+\Sigma_2^3 \alpha_i \nu^i)^2 & \text{for } f_s < f_{merg}, \\ f_s w_m (1+\Sigma_1^2 \epsilon_i \nu^i)^2 & \text{for } f_{merg} \leq f_s < f_{ring}, \\ f_s^{1/3} w_r \mathcal{L}^2(f_s, f_{ring}, \sigma) & \text{for } f_{ring} \leq f_s < f_{cut}, \end{cases}$$

where

(i) $\frac{dE_{GW}^{Newton}(f_s)}{df_s} = \frac{5}{12}(G\pi)^{2/3}\mathcal{M}_c^{5/3} F_\theta f_s^{-1/3}$,
(ii) $F_\theta = \frac{(1+\cos^2\theta)^2}{4} + \cos^2\theta$,
(iii) $\nu = \frac{(\pi G M f_s)^{1/3}}{c}$, and
(iv) $\mathcal{L}(f, f_{ring}, \sigma) = \frac{\sigma}{2\pi[(f-f_{ring})^2 + 0.24\sigma^2]}$. w_m, and w_r are the continuity coefficients.

The coefficients α_i and ϵ_i are given in Ajith et al. (2008); with our null assumption for the spin ($\chi = 0$), they can be written as $\epsilon_1 = -1.8897$, $\epsilon_2 = 1.6557$, $\alpha_2 = -\frac{323}{224} + \frac{451}{168}\eta$, and $\alpha_3 = 0$, with $\eta = \frac{M_1 M_2}{M^2}$.

The phase transition frequencies f_{merg}, f_{ring}, f_{cut}, and σ are calculated as (Ajith et al. 2008)

$$\frac{\pi G M}{c^3}\mu_k = \mu_k^0 \text{ with } \mu_k = (f_{merg},\ f_{ring},\ f_{cut},\ \sigma),$$

where the coefficients μ_k^0 are given in table I of Ajith et al. (2011); for $\chi = 0$, we get the following:

μ_k	μ_k^0
f_{merg}	0.066
f_{ring}	0.185
f_{cut}	0.3236
σ	0.925

This paper has been typeset from a TEX/LATEX file prepared by the author.